JOURNAL OF APPLIED CRYSTALLOGRAPHY
ISSN 1600-5767

3D printed droplet generation devices for serial femtosecond crystallography enabled by surface coating

Austin Echelmeier,[a,b]‡ Daihyun Kim,[a,b]‡ Jorvani Cruz Villarreal,[a,b] Jesse Coe,[a,b] Sebastian Quintana,[a,b] Gerrit Brehm,[c] Ana Egatz-Gomez,[a,b] Reza Nazari,[b,d] Raymond G. Sierra,[e] Jason E. Koglin,[e] Alexander Batyuk,[e] Mark S. Hunter,[e] Sébastien Boutet,[e] Nadia Zatsepin,[b,d] Richard A. Kirian,[b,d] Thomas D. Grant,[f] Petra Fromme[a,b] and Alexandra Ros[a,b]*

[a]School of Molecular Sciences, Arizona State University, Tempe, Arizona, USA, [b]Center for Applied Structural Discovery, The Biodesign Institute, Arizona State University, Tempe, Arizona, USA, [c]Institute for X-ray Physics, University of Göttingen, Göttingen, Germany, [d]Department of Physics, Arizona State University, Tempe, Arizona, USA, [e]Linac Coherent Light Source, SLAC National Accelerator Laboratory, 2575 Sand Hill Road, Menlo Park, California 94025, USA, and [f]Hauptman-Woodward Institute, Department of Structural Biology, Jacobs School of Medicine and Biomedical Sciences, SUNY University at Buffalo, Buffalo, New York, USA. *Correspondence e-mail: alexandra.ros@asu.edu

Received 23 January 2019
Accepted 19 July 2019

Edited by A. Barty, DESY, Hamburg, Germany

‡ These authors contributed equally

Keywords: microfluidic devices; serial crystallography; injection; droplet generation.

Supporting information: this article has supporting information at journals.iucr.org/j

The role of surface wetting properties and their impact on the performance of 3D printed microfluidic droplet generation devices for serial femtosecond crystallography (SFX) are reported. SFX is a novel crystallography method enabling structure determination of proteins at room temperature with atomic resolution using X-ray free-electron lasers (XFELs). In SFX, protein crystals in their mother liquor are delivered and intersected with a pulsed X-ray beam using a liquid jet injector. Owing to the pulsed nature of the X-ray beam, liquid jets tend to waste the vast majority of injected crystals, which this work aims to overcome with the delivery of aqueous protein crystal suspension droplets segmented by an oil phase. For this purpose, 3D printed droplet generators that can be easily customized for a variety of XFEL measurements have been developed. The surface properties, in particular the wetting properties of the resist materials compatible with the employed two-photon printing technology, have so far not been characterized extensively, but are crucial for stable droplet generation. This work investigates experimentally the effectiveness and the long-term stability of three different surface treatments on photoresist films and glass as models for our 3D printed droplet generator and the fused silica capillaries employed in the other fluidic components of an SFX experiment. Finally, the droplet generation performance of an assembly consisting of the 3D printed device and fused silica capillaries is examined. Stable and reproducible droplet generation was achieved with a fluorinated surface coating which also allowed for robust downstream droplet delivery. Experimental XFEL diffraction data of crystals formed from the large membrane protein complex photosystem I demonstrate the full compatibility of the new injection method with very fragile membrane protein crystals and show that successful droplet generation of crystal-laden aqueous droplets intersected by an oil phase correlates with increased crystal hit rates.

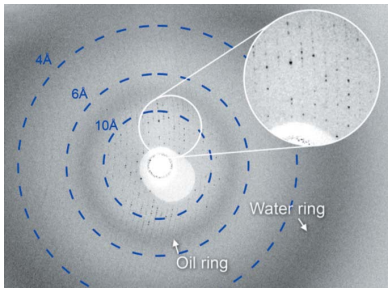

1. Introduction

X-ray crystallography is one of the most powerful tools to elucidate protein structures. High-intensity femtosecond X-ray free-electron lasers (XFELs) allow for the investigation of protein structure and dynamics with atomic resolution. Unlike traditional X-ray crystallography where a single protein crystal is rotated and irradiated with X-rays, in serial femtosecond crystallography (SFX) a protein structure is

determined by merging thousands of diffraction patterns from individual micro- and nanometre-sized crystals being 'hit' by the XFEL pulses in random orientations (Chapman *et al.*, 2011). The crystals need to be rapidly replenished because they are destroyed by the XFEL beam in less than a picosecond. A major method to accomplish crystal delivery is by jetting an aqueous suspension of protein crystals across the beam path using a gas dynamic virtual nozzle (GDVN) (Doak *et al.*, 2012; Trebbin *et al.*, 2014). Although the femtosecond X-ray pulses of XFELs either have varying repetition rates from 30 Hz up to 120 Hz or arrive in 10 Hz bunch trains with each bunch containing up to 2700 X-ray pulses (Chavas *et al.*, 2015; Seddon *et al.*, 2017), every XFEL beamline has a common problem: crystals injected between pulses or bunch trains are not irradiated and are therefore wasted. The sample cannot be recycled as the radicals formed by the XFEL beam exposure spread the damage in the solution. Large protein amounts, up to millilitres of protein crystal suspension, or tens of milligrams to grams of protein, are then required to obtain a complete data set (Martin-Garcia *et al.*, 2016). Methods for producing and crystallizing proteins in such large amounts are highly resource and time intensive and can be a serious limiting factor for protein crystallography with XFELs. Thus, methods for reducing protein crystal waste in serial femtosecond crystallography are of the utmost importance. Examples of sample-introduction methods with reduced sample consumption (Martin-Garcia *et al.*, 2016; Martiel *et al.*, 2019) are viscous media injection (Weierstall, 2014; Sugahara *et al.*, 2015, 2016; Conrad *et al.*, 2015), electrospinning with a microfluidic electrokinetic sample holder injector (Sierra *et al.*, 2016), double flow-focusing nozzles (Oberthuer *et al.*, 2017), acoustic droplet ejection (Mafune *et al.*, 2016; Roessler *et al.*, 2016), droplet on tape (Fuller *et al.*, 2017) and fixed target (Heymann *et al.*, 2014; Hunter *et al.*, 2014; Lyubimov *et al.*, 2015; Mathews *et al.*, 2017; Mueller *et al.*, 2015; Murray *et al.*, 2015; Roedig *et al.*, 2017). In addition, recirculating jets that recycle the injected sample have been developed and employed at the Linac Coherent Light Source (LCLS) (Hunter & Sublett, 2019) and the SPring-8 Ångstrom Compact Free Electron Laser (SACLA) (Tono *et al.*, 2015; Tono, 2017). However, the recirculating jet setup at LCLS is not designed for experiments under vacuum, and jet diameters are typically $\geq$20 µm, both contributing to higher background scattering than non-recirculating jets under vacuum. Furthermore, SACLA requires a minimum sample volume of 5 ml in order to use the recirculating jet, a volume which can be prohibitive for samples that are difficult to crystallize in large volumes. The exposure to the XFEL beam also leads to ionization and radical formation, inducing damage in the recycled sample even if the protein crystals have not been exposed to a laser pulse. Such radiation damage defers the goal of SFX for near-damage-free X-ray diffraction collection from protein crystals at room temperature such as metal proteins like photosystem I (PSI), but recycling jets may still be applied for radiation-hard samples.

Microfluidic devices have been explored in traditional crystallography applications typically coupled with synchrotron irradiation (Zheng *et al.*, 2004; Ghazal *et al.*, 2016; Maeki *et al.*, 2016), and also in crystallography with XFELs including microfabricated liquid jet injectors (Trebbin *et al.*, 2014; Beyerlein *et al.*, 2015), crystal sorters (Abdallah *et al.*, 2013) and time-resolved crystallography with microfluidic mixers (Calvey *et al.*, 2016). We have recently proposed using water-in-oil microfluidic droplets to reduce the protein crystal suspension volume for SFX with XFELs (Echelmeier *et al.*, 2015). For droplet generation we fabricated a device using two-photon polymerization 3D printing. This approach involves a polymerization reaction initiated by near-infrared femtosecond laser pulses focused into a photosensitive material volume, followed by the removal of non-photopolymerized material, with advantages including micrometre resolution, availability of transparent photoresists and fast design modification (Waheed *et al.*, 2016; Lee *et al.*, 2008). This 3D printing approach has been utilized to develop nozzles for SFX sample delivery (Bohne *et al.*, 2019; Nelson *et al.*, 2016; Wiedorn *et al.*, 2018). Although droplets can be generated using devices with different geometries, we have focused on a T-junction geometry because of its simplicity and well characterized droplet formation physical parameters (Thorsen *et al.*, 2001; Nisisako *et al.*, 2002; Zheng *et al.*, 2003; Song & Ismagilov, 2003; Song *et al.*, 2003; Li & Ismagilov, 2010; Garstecki *et al.*, 2006; Husny & Cooper-White, 2006; Zhu & Wang, 2016). In T-junction droplet generators, the continuous-phase channel orthogonally intersects the dispersed-phase channel, and the resulting droplets proceed down the continuous-phase channel outlet (Husny & Cooper-White, 2006).

Generation of multiphase flows in XFEL experiments poses unique challenges unlike those in droplet generation in microfluidic devices at low pressure. Firstly, the sample is placed in a reservoir which frequently requires a few metres of liquid lines to connect to the GDVN. This connection is established through fused silica capillaries with small inner diameters (50–100 µm) and is required for accommodating protein crystal suspension anti-settling devices necessary to avoid clogging. Therefore, fluidic resistance is high, and pressures comparable to those typical in high performance liquid chromatography (HPLC) are usually required for the crystal suspension injection. Polyether ether ketone (PEEK) devices withstand high operating pressures and have been used for droplet generation with controlled droplet frequency by adjusting the flow rate ratios of the two phases employed for droplet generation, from hundreds of microlitres to millilitres per minute (Ferreira *et al.*, 2018; Zhang *et al.*, 2015). However, because of their relatively large internal diameters they do not allow for adjustment of droplet volumes and frequencies within the much lower flow rates typical for SFX (tens of microlitres down to hundreds of nanolitres per minute), as we noted in preliminary tests. In addition, PEEK devices are not transparent and do not allow visual monitoring of the droplet generation.

Second, wetting properties are crucial for reproducible and long-term droplet generation in an SFX experiment and have not been fully investigated. An ideal coating should render

hydrophobic both the 3D printed photoresist droplet generator and the upstream and downstream fused silica capillary surfaces. Also, it is highly desirable to collect diffraction data uninterruptedly for typically 6–12 h over the course of one shift at the XFEL beamline. Surface coatings should therefore be stable over long periods at flow rates of tens of microlitres per minute.

A huge variety of coating methods on photoresists and glass have been developed, addressing surface composition, chemical functionality, wettability, charge, porosity/roughness and coating durability, including coating methods to impart specific wetting properties in microfluidic droplet generation devices (Ho *et al.*, 2015; Waheed *et al.*, 2016). Droplet formation occurs when the drag force, with a minor contribution from inertia, overcomes the interfacial tension. However, coating the inner surface of an SFX device assembly consisting of a 3D printed droplet generator with internal dimensions of a few tens of micrometres connected to several metres-long fused silica capillaries with internal diameters between 50 and 100 µm can be extremely challenging and time consuming. Chemical approaches for surface modification such as self-assembled monolayers (Wong & Ho, 2009) and gas-phase silanization methods (Fadeev & Kazakevich, 2002; Wong & Ho, 2009) typically require an activation step (Fadeev & Kazakevich, 2002; Wong & Ho, 2009), *e.g.* acid or plasma treatment, for rendering desired surface chemical functionality prior to the linking reaction. Silanization under a vapor environment in addition involves a relatively complicated setup (Fadeev & Kazakevich, 2002) (*e.g.* vacuum and ventilation system) and protocol. Fluorophilic surface coatings in cyclic olefin copolymer microfluidic devices for fixed-target crystallography were achieved using a simple protocol (Aghvami *et al.*, 2017). All these surface coating methods, while effective for microfluidic devices with dimensions of a few millimetres, would be highly impractical to use with our device assemblies, which include a glass nozzle, metres of silica capillaries and the 3D printed droplet generator device, and too cumbersome to perform if needed during beamtime experiments. Therefore, we explored simpler physical adsorptive coatings and tested them on various surfaces, including photoresists used in two-photon polymerization 3D printing approaches as well as on glass surfaces (del Campo & Greiner, 2007; Huang *et al.*, 2015; Ligon *et al.*, 2017; Nelson *et al.*, 2016; Wiedorn *et al.*, 2018).

We have addressed challenges in droplet generation for SFX by developing a 3D printed microfluidic droplet generator with a size <2 mm in every dimension, which can withstand high pressures (up to approximately 2500 psi; 1 psi = 6.89 kPa), is transparent and can be rapidly prototyped. In addition, our device is compatible with both low and high X-ray pulse frequencies (from 10 to 120 Hz), supports micro- to nano-sized crystals, does not ionize the protein crystal, and is suitable for time-resolved serial crystallography. Here we investigate different adsorptive surface coatings that can produce and maintain stable droplet streams for several hours under high pressure in device assemblies for droplet generation in SFX experiments and assess the ability to collect XFEL diffraction data from droplets of PSI protein crystal suspensions.

2. Materials and methods

2.1. Reagents and materials

Silicon wafers (p-type ⟨100⟩, 4 inches) were obtained from University Wafer, USA. Glass slides (76 × 25 × 1 mm) were purchased from Fisher Scientific, USA. The negative photoresist SU-8 2007 for surface coating and SU-8 developer were purchased from Microchem, USA. The ultraviolet sensitive photoresist (IP-S) was purchased from Nanoscribe GmbH, Germany. (Tridecafluoro-1,1,2,2-tetrahydrooctyl) dimethylchlorosilane (TDTS) was purchased from Gelest Corp., USA. Novec 1720 electronic grade was a generous gift from 3M, USA. Aculon AL-B was purchased from Aculon Inc., USA. Ethanol, acetone, potassium chloride, magnesium sulfate, Tris base, 2-(*N*-morpholino)ethanesulfonic acid (MES), *β*-mercaptoethanol, poly(ethylene glycol) methyl ether (mPEG, MW = 5000 amu), perfluorodecalin (PFD) and 1*H*,1*H*,2*H*,2*H*-perfluoro-1-octanol (perfluorooctanol, PFO) were purchased from Sigma–Aldrich, USA. *n*-Dodecyl-*β*-maltopyranoside was purchased from Glycon, Germany. Deionized water (18 MΩ) was supplied from a Synergy purification system (Millipore, USA). Fused silica capillaries (360 µm outer diameter, 100 µm inner diameter and 50 µm inner diameter) were purchased from Molex, USA. Hardman extra-fast setting epoxy was purchased from All-Spec, USA.

2.2. Preparation of photoresist film model surfaces

Silicon wafers and glass slides were sonicated in isopropanol and acetone for 5 min and immediately rinsed thoroughly with deionized water and dried with a stream of nitrogen gas before the surface coating. A previously described SU-8 coating method was used (Duong *et al.*, 2003). In brief, an Si wafer was spin-coated at 1000 r min^{-1} with a Laurell spinner (WS-650–8, Laurell, USA) for 30 s by dispensing 3 ml of negative photoresist SU-8, UV-exposed for 30 s (350 W, 10.32 mW cm^{-2}, HTG Mask Aligner, JM Industries, USA) and developed in a developer bath. The thickness of the SU-8 film was 12 µm as measured by a profilometer (Dektak II, USA). The IP-S photoresist was spin-coated at 1000 r min^{-1} for 60 s on a silicon wafer and then cured by a high-power UV (365 nm) curing LED system (CS2010, Thorlabs, USA) under an inert N_2 atmosphere. The thickness of the IP-S layer on the Si wafer was 62 µm as measured by the Dektak profilometer.

2.3. Hydrophobic coatings on photoresists and glass

SU-8 or IP-S films on silicon wafers and bare glass slides were coated with hydrophobic agents as follows. The surfaces were rinsed with deionized water and dried with a stream of nitrogen gas and placed in glass Petri dishes. A volume of 200 µl of either Novec 1720 or Aculon AL-B was placed on the substrate and allowed to evaporate at room temperature. Subsequently, the substrates were baked in an oven at 423 K for 30 min. For the surface coating with a fluorinated silane,

gas-phase deposition of TDTS was performed in a desiccator connected to a vacuum source by evaporating 40 µl of TDTS in an incubator with SU-8 and IP-S substrates. A vacuum was applied for 1 min then turned off and the TDTS was allowed to deposit for 30 min.

2.4. Contact angle measurement

All substrates were rinsed with deionized water and dried with compressed air or nitrogen gas before measurement. Contact angles were measured with a goniometer (drop shape analyzer DSA25, Kruss, Germany) under ambient conditions. To measure the static water contact angle, a sessile drop (2 µl) of deionized water was dispensed onto bare and treated photoresist films and glass slides, and a side image was captured with the camera when the droplet was stabilized on the substrate. Three different samples for each material and surface treatment were measured.

2.5. Stability of hydrophobic coatings

To explore the long-term coating stability we measured the contact angles on Novec 1720-treated SU-8, IP-S and glass slides before and after immersion in either a mixture of PFD:PFO (10:1 *v*:*v*%) oil for up to 24 h or ethanol or deionized water for up to 16 h. In addition, the contact angles of the Novec-treated samples were measured before and after immersion in deionized water in an ultrasonic bath (JP-031B 180 W, 40 K Hz, 6.5 L, USA) for 3, 10 and 30 min at room temperature followed by drying under pressurized N_2 gas.

2.6. 3D printed devices for droplet generation

Devices were designed in *AutoCAD* (AutoDesk, USA) and imported into the *DeScribe* software of the Nanoscribe GT instrument (Nanoscribe GmbH, Germany). A drop of IP-S was deposited onto a clean indium tin oxide-coated boroaluminosilicate glass slide. The 3D structure was printed on the glass slide upon the two-photon polymerization of IP-S. The structure was printed using the standard Meso Scale protocol: IP-S 25x solid (ITO) recipe, with 100 000 µm s^{-1} scan speed, 100% laser power, 0.9 power scaling, 1 µm slice distance and 0.5 µm hatch distance. Printing was complete after 4–7 h depending on the device version. After printing, the device was developed by one or more cycles of a 40 min sonication in SU-8 developer followed by an isopropyl alcohol rinse until development completion was determined by visual inspection using an optical microscope. After development, the dry 3D printed device was immobilized on a glass slide with tape, and 360 µm outer diameter fused silica capillaries with polished flat ends were inserted into the two inlets and the outlet of the device. The diameters of the two inlet and the outlet ports were 370 µm. Fused silica capillaries were permanently affixed to the device with fast-curing epoxy for high-pressure operation.

2.7. T-junction and capillary coating with Novec 1720

For hydrophobic surface treatment, Novec 1720, as provided by the manufacturer, was slowly injected into one of the T-junction assembled capillaries using a disposable syringe and fittings (P-629, F-300, F-142N and F-262) (IDEX-HS, USA) until it could be seen exiting the other two fused silica capillary ends. The entire Novec-filled assembled device was placed in a ventilated oven at 423 K overnight to allow for vaporization of any excess solvent.

2.8. Droplet generation and monitoring

The oil-phase mixture was PFD:PFO (10:1 *v*:*v*%). The aqueous phase was either water, mPEG buffer (82 m*M* potassium chloride, 14 m*M* Tris base pH = 7.3, 1.4 m*M* β-mercaptoethanol and 7% mPEG, used as mother liquor for the protein of interest for SFX studies) or low ionic strength PSI buffer [5 m*M* MES pH = 6.4 and 0.02%(*w*/*v*) *n*-dodecyl-β-maltopyranoside] for delivery of PSI crystals. In the X-ray diffraction experiments the aqueous phase was a suspension of 1–5 µm PSI protein microcrystals prepared as described previously (Chapman *et al.*, 2011; Abdallah *et al.*, 2015; Hunter & Fromme, 2011), and the aqueous phase reservoir was mounted on a custom-made device that slowly oscillates to prevent microcrystals from settling while keeping the crystal suspension at 277 K (Lomb, 2012). The aqueous and oil phases were each driven by an HPLC pump (LC-20AD, Shimadzu, Japan) operating in constant-flow-rate mode into a custom-made stainless steel syringe-like reservoir (Oberthuer *et al.*, 2017; Wang, 2014). The reservoirs were connected to the 3D printed T-junction microfluidic droplet generator by fused silica capillaries. Oil-phase flow rates (Q_{oil}) ranged from 6 to 45 µl min^{-1}, and aqueous-phase flow rates ($Q_{aqueous}$) from 0.5 to 20 µl min^{-1}. The outlet capillary was mounted in a droplet detector about 30 cm downstream of the droplet generator, and about 20 cm further downstream was connected to the GDVN inlet liquid capillary. For preliminary studies at the laboratories at Arizona State University prior to the first experiments at the Linac Coherent Light Source (LCLS) at SLAC National Accelerator Laboratory, the T-junction droplet generation was imaged by immobilizing the 3D printed device onto a glass slide with tape and using an inverted microscope (IX71, Olympus, USA) in bright-field imaging mode in conjunction with a high-speed camera (FASTCAM SA4, Photron, Japan). The droplet detector was used to monitor the frequency of the droplets in real time in the fused silica capillary and consisted of a 1550 nm laser diode and a photodetector connected to an oscilloscope, which detected a signal based on the difference in transmittance between the oil and the aqueous phase.

2.9. X-ray diffraction

The SFX experiments were carried out at the macromolecular femtosecond crystallography (MFX) instrument at LCLS (proposal ID: LQ70) at an X-ray energy of 9.5 keV with 40 fs pulse duration at a pulse rate of 120 Hz (Sierra *et al.*, 2019). The X-ray diffraction experiments were carried out at ambient pressure in a helium atmosphere to reduce background scattering from air. The X-ray diffraction data were recorded using a Rayonix MX170-HS detector in the 2 × 2

binning mode, leading to 1920 × 1920 pixels, each 89 × 89 µm. In this mode, the rate of data collection was detector-limited to 10 Hz. For online data collection monitoring and live real-time crystal hit rates, we used *OnDA* (Mariani *et al.*, 2016). Further analysis was performed on a single experimental run where we observed droplet generation as detected by the above mentioned droplet detector during beamtime. The images were preprocessed to detect the crystal hits using *Cheetah* (Barty *et al.*, 2014). To identify when aqueous-phase droplets formed, based on the X-ray scattering, we used radial profiles calculated from each 2D image to distinguish the aqueous-phase scattering from the largely different oil-phase scattering. The radial profiles from oil-only and water/aqueous-buffer-only data were calculated and used for estimating volume fractions of oil and water in each PSI diffraction image (where volume fraction of water + volume fraction of oil = 1.0). Volume fractions (Boutet *et al.*, 2016) were estimated using a linear combination of oil and water scattering profiles with custom Python scripts. Images were sorted by increasing fractions of water and the crystal hit rate was calculated by binning the sorted images into groups of 100 images.

3. Results and discussion

The wetting properties of the channels are crucial for the quality and reproducibility of droplet generation. For producing water-in-oil droplets, the device walls need to be hydrophobic, whereas oil-in-water droplets require hydrophilic channels (Chae *et al.*, 2009; Seemann *et al.*, 2012; Teh *et al.*, 2008). Since the wetting properties of the employed Nanoscribe proprietary photoresist have not been studied in detail, we investigated the effect of different hydrophobic surface treatments on 3D printed device assemblies with regards to droplet generation performance in SFX.

3.1. Device fabrication and characteristics

A schematic of droplet generation in a microfluidic T-junction is shown in Fig. 1. In a hydrophobic channel [Fig. 1(*a*)] the oil coats the walls of the T-junction and prevents aqueous-phase adherence and, as the aqueous phase extends into the oil channel, droplets pinch off the bulk and proceed downstream to the outlet. In contrast, in a hydrophilic channel [Fig. 1(*b*)] the aqueous phase adheres to the walls and co-flows with the oil without breaking into droplets. These effects can also be seen in a fused silica capillary [as demonstrated below in Fig. 5(*d*)]. A computer-aided design (CAD) drawing and an optical microscopy bright-field image of the 3D printed droplet generator are shown in Figs. 1(*c*) and 1(*d*), respectively. The oil enters through the left side of the device into the large rectangular channel of the T-junction (width = 100 µm, height = 75 µm), while the aqueous phase enters through a circular channel (radius = 25 µm) orthogonal to the oil channel. Flow proceeds down the large channel toward the outlet port (right). All three ports are connected to 360 µm fused silica capillaries and are sealed with epoxy to withstand high pressures. This seal can typically withstand sustained pressure of several hundred psi over a time period of 12 h, with short-durations of increased pressure up to 2500 psi, as demonstrated during an SFX shift.

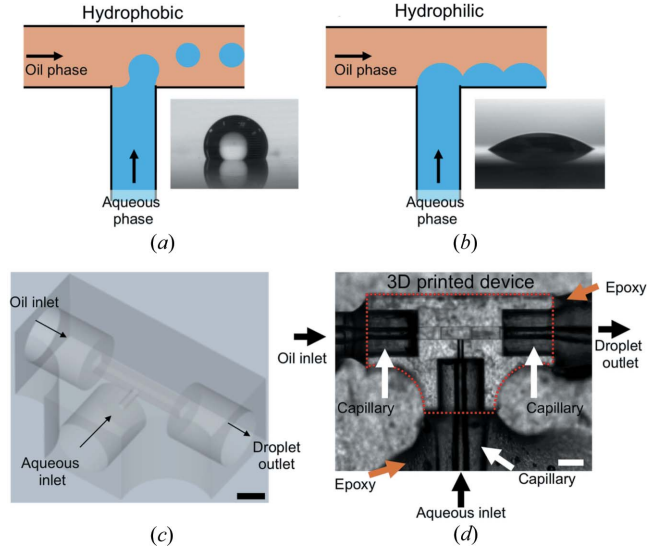

Figure 1
(*a*) Schematic of ideal water-in-oil droplet generation in a T-junction device with hydrophobic walls. Inset: image of a water droplet sitting on glass treated with a hydrophobic coating agent. (*b*) Schematic of a hydrophilic T-junction droplet generation device. The aqueous phase adheres to the walls and oil flows beside it; no droplets are generated. Inset: image of a water droplet on a hydrophilic glass slide. Panels (*a*) and (*b*) are not to scale. (*c*) CAD drawing of the 3D printed droplet generator. The black arrows indicate the various inlets and outlet. (*d*) Bright-field microscopy image of a 3D printed droplet generator (red dotted outline), epoxy-bonded and connected to fused silica capillaries. White arrows indicate capillaries and orange arrows indicate epoxy bonding material. The gray speckled background is due to tape used to attach the device onto a glass slide for microscopy. Scale bars in (*c*) and (*d*) are 200 µm.

3.2. Glass and photoresist treatment with different fluorinated agents

Fluorinated agents for treatment of microfluidic droplet generators include perfluorinated polymers (Nge *et al.*, 2013; Martinelli *et al.*, 2008; Sarvothaman *et al.*, 2015), long fluorinated hydrocarbon compounds such as polyfluoropolyethers (Riche *et al.*, 2014; Kuhn *et al.*, 2011) and commercialized adsorptive fluoropolymer surfactants (Tullis *et al.*, 2014; Scheler *et al.*, 2016; Guzowski *et al.*, 2016). Our goal was to investigate the stability of the droplet streams in a serial crystallography setup using a 3D printed droplet generator with three different adsorptive surface coatings. Owing to their geometry and small dimensions, it is not possible to measure contact angles inside fused silica capillaries and 3D printed devices using a sessile droplet. Instead, we investigated static water contact angles on borosilicate glass slides as well as on SU-8 and IP-S films spin-coated on silicon wafers before and after applying three different fluorinated hydrophobic surface treatments to mimic the coating effect within fused silica capillaries and 3D printed T-junction channels, respectively.

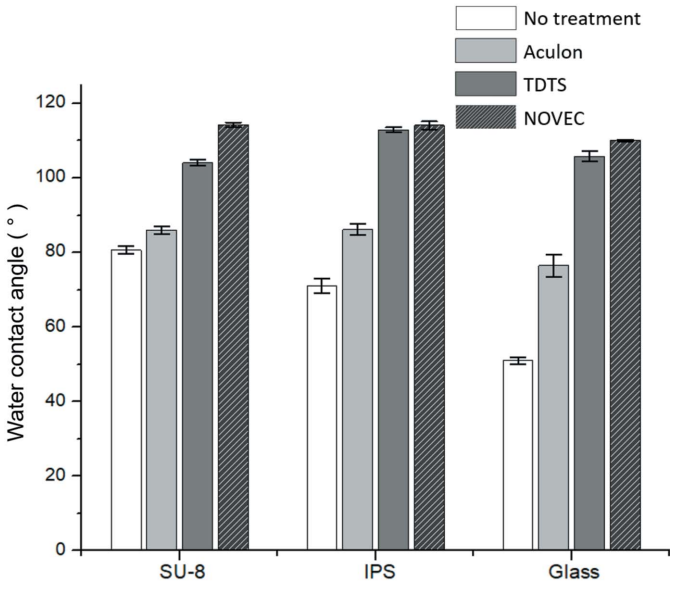

Figure 2
Static water contact angle (θ) measurements on SU-8, IP-S and glass substrates before and after treatment with three fluorinated chemicals. Error bars represent the standard deviations of the mean contact angle measurements.

Novec and Aculon are two commercially available long-chain fluorinated hydrocarbons, both dissolved in methyl nonafluorobutyl ether and methyl nonafluoroisobutyl ether. Aside from solvent composition, they presumably also differ in the fluorinated compound content, which is a trade secret. Both are specified for water repellent treatment and can be flowed through microfluidic channels and capillaries for easy application (Novec 1720 EGC Technical Data Sheet and Aculon AL-B Technical Data Sheet; available at https://www.3m.com). The third agent, TDTS, was applied through chemical vapor deposition. All treatment agents produced an increase in contact angle on the three surfaces tested, but to a different extent. The contact angle measurements and corresponding droplet images are shown and listed in Fig. 2(*a*) and the supporting information.

For our application, Novec was the most advantageous treatment. It was easiest to handle – specifically as simply flushing it through the device treats the inner surfaces of the 3D printed droplet generator assembled with silica capillaries. Furthermore, it produced the largest contact angles $\theta \geq 110^{\circ}$ for all three substrates and demonstrated good long-term stability, as detailed in the following section. Silanization with

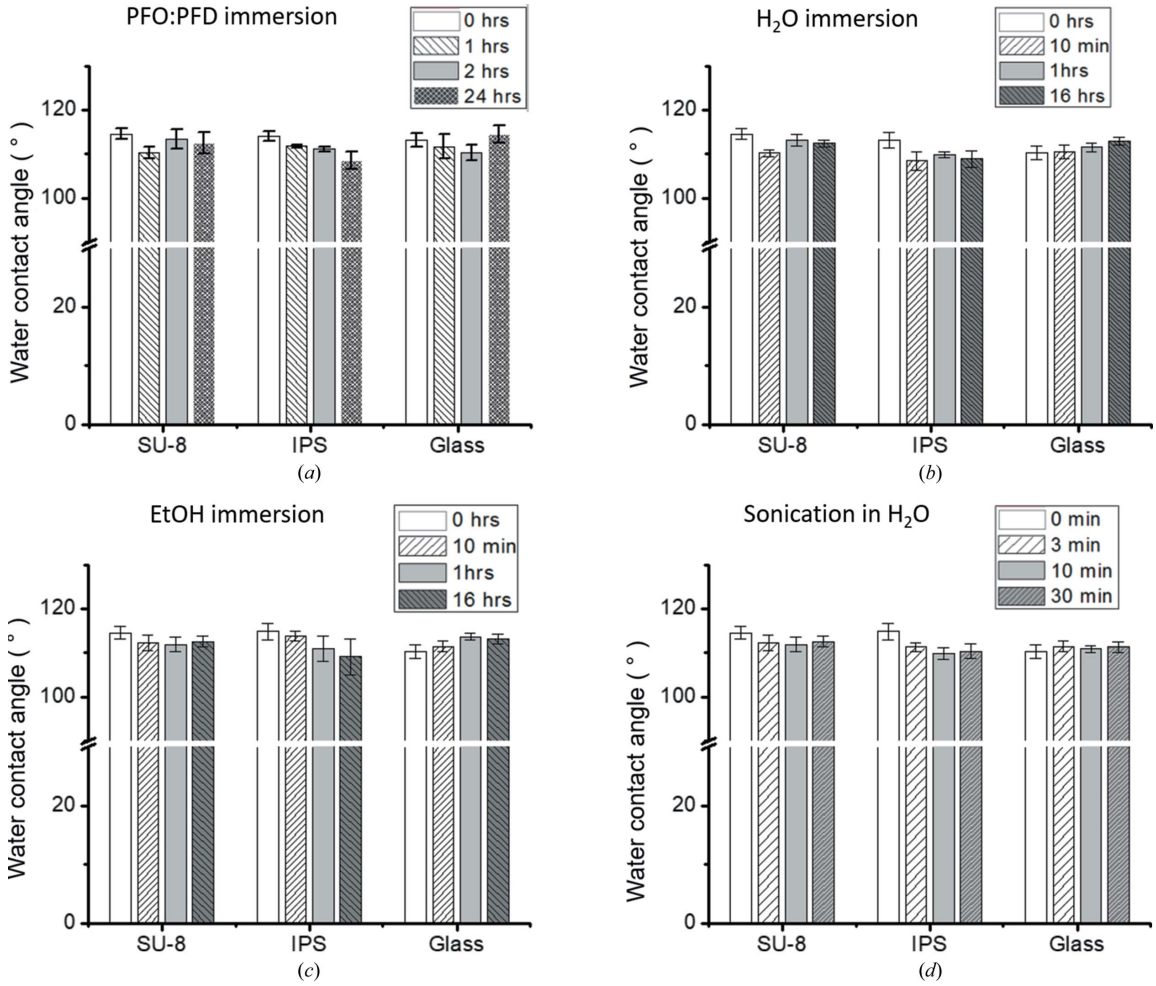

Figure 3
Stability of Novec coating on SU-8, IPS and glass substrates subject to various conditions. The measurements were obtained by immersing the Novec-coated substrates in (*a*) PFD:PFO (10:1 *v*:*v*%) for up to 24 h, (*b*) deionized water for up to 16 h and (*c*) ethanol (EtOH) for up to 16 h and (*d*) ultrasonication in deionized water for up to 30 min.

TDTS produced contact angles almost as large as Novec, although for our particular application this method presented several disadvantages. Introducing TDTS in the gas phase into 3D printed devices with a few hundred micrometre-sized inner diameters coupled to long fused silica capillaries is cumbersome to accomplish. In addition, for optimum results silanization requires an activation step with plasma (Saini *et al.*, 2008) or acid (Fadeev & Kazakevich, 2002) to increase the number of hydroxyl groups on the surface before surface modification. Since activation of the inner surface of our assembled devices with plasma is not feasible, and activation with acid would be cumbersome and could damage our devices, we did not further consider this method. Finally, the Aculon treatment did not produce hydrophobic ($\theta > 90^\circ$) surfaces on any of the substrates.

Compared with smooth spin-coated films, the walls of the IP-S 3D printed device may present a higher surface roughness depending on printing parameters such as the objective magnification, slicing distance and hatching distance. For the described 3D printed T-junctions, the root-mean-square roughness amplitude is estimated to be on the order of 100 nm (Kirchner *et al.*, 2017). The effect of roughness on the wetting properties in the meso-scale (several hundreds of micrometres to millimetres) typically amplifies the hydrophilic or hydrophobic character of the corresponding smooth surface (Quéré, 2008). For two-phase flows in hydrophilic microfluidic channels, such as the 3D printed devices without surface treatment or with Aculon coating, the effect of the contact line pinning at surface irregularities can decrease its intrinsic hydrophilicity (Yang *et al.*, 2018). In a hydrophobic channel, such as Novec-coated IP-S devices (Fig. 2), the effect of the surface roughness is always further increased by the surface hydrophobicity (Yang *et al.*, 2008) and thus is advantageous for the generation of water-in-oil droplets.

3.3. Long-term hydrophobic coating stability tests

In SFX experiments with XFELs, protein crystal suspensions are delivered to the X-ray beam for several hours, and thus the surface coating stability is critical for sustained droplet generation. To determine whether the Novec-modified surfaces can retain their hydrophobicity, we investigated the treatment stability under various conditions. We mimicked the flow conditions in a droplet generator by immersing Novec-coated SU-8, IP-S and glass surfaces in various solvents, and also by sonicating the samples for 3–30 min in water. Fig. 3 shows contact angle measurements on Novec-treated SU-8, IP-S and glass surfaces before and after various immersion times in oil, deionized water and ethanol, and after sonication in water. The measured contact angles did not exhibit noticeable changes, which indicates that the Novec treatment is effective in rendering SU-8, IP-S and glass surfaces hydrophobic, with excellent long-term stability. The excellent stability of the surface coating with Novec was also observed during droplet generation in an SFX experiment, as discussed below.

3.4. Effects of surface treatment on droplet generation

Next, we compared the effects of the hydrophobic surface treatment on the droplet generation behavior of T-junction devices assembled with fused silica capillaries. The experimental setup used at the MFX instrument is described in detail in the experimental section and schematically shown in Fig. 4. This setup was mimicked in laboratory experiments, with similar flow rates, pressures, tubing and capillary lengths, and coupling the droplet generator and GDVN. In this setup, droplets of protein crystal suspensions could be generated reproducibly using a single T-junction device for periods of ∼8 h under applied pressures from ∼200 psi up to 2500 psi (for short periods of pressure spikes), with protein crystal suspension flow rates of 1–5 µl min^{-1} and total flow rates of 20–40 µl min^{-1}. The high pressure arises from the long lengths of small-inner-diameter capillaries and the viscosity of the oil phase; for example, for a conservative length of 1 m, an inner diameter of 50 µm and viscosity of 5.1 cP for PFD, the pressure drop required is approximately 1500 psi. The frequency of the droplets ranged from 30 to 150 Hz depending on the flow rates of the aqueous and oil phases.

We first characterized the fluid-flow behavior on the IP-S and fused silica capillary portions of the fully assembled device, as summarized in Fig. 5. When the droplet generator assembly was left untreated, no droplets could be generated. The aqueous phase streamlines along the surfaces, randomly making contact with the device walls, and varying the flow rate Q did not disrupt the stability of the streamlines. This situation is depicted in Fig. 5(*a*) for Q_{oil} = 10 µl min^{-1} and $Q_{aqueous}$ = 5 µl min^{-1}. When the droplet generator assembly was treated with Aculon, droplets usually appeared in the 3D printed device initially; however, after a few minutes under flow, the aqueous phase began adhering to the wall, streamlining and

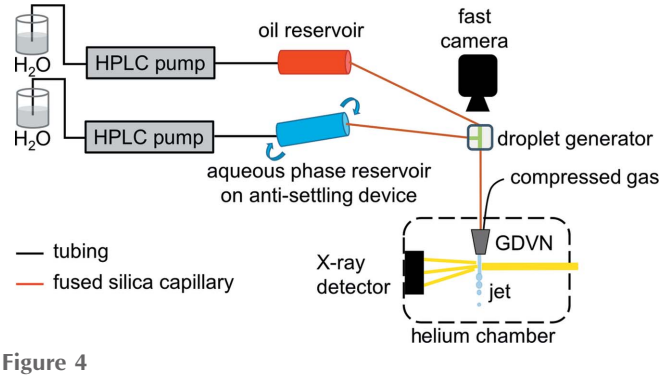

Figure 4
Experimental setup for droplet generation. Two HPLC pumps were used to drive two stainless steel reservoirs containing the oil and aqueous phases. The aqueous phase reservoir was mounted in a slowly oscillating holder (represented by curved arrows) to prevent the crystals from settling. The reservoirs were connected to the T-junction droplet generator using fused silica capillaries. Droplet generation at the T-junction was imaged using bright-field microscopy coupled to a fast camera. The outlet of the droplet generator was connected to a droplet detector and subsequently to the GDVN using a fused silica capillary. Helium gas was used in the GDVN to form a stable jet. The droplet detector consisted of a 1550 nm laser diode and a photodetector connected to an oscilloscope. Based on the differences in transmittance between oil and water at this wavelength, the droplet frequency was monitored.

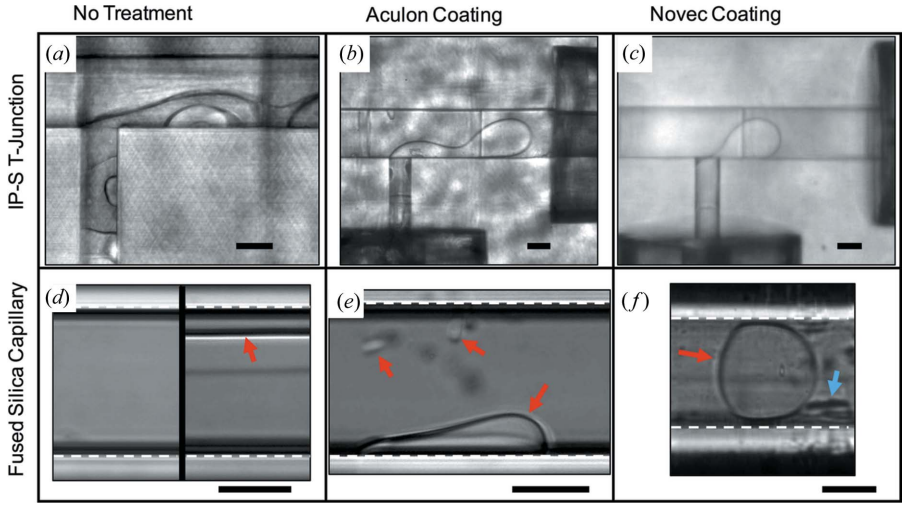

Figure 5
Effect of surface treatment on IP-S (*a*)–(*c*) and fused silica (*d*)–(*f*) capillaries on water-in-oil droplet generation. For IP-S: (*a*) no surface treatment ($\theta < 90^\circ$) results in the aqueous phase forming streamlines instead of droplets (Q_{oil} = 10 µl min^{-1}; $Q_{aqueous}$ = 5 µl min^{-1}), (*b*) surface treatment with Aculon ($\theta < 90^\circ$) results in adherence of the aqueous phase to IP-S until it pinches off into a droplet at the T-junction capillary joint (Q_{oil} = 12 µl min^{-1}; $Q_{mPEG\ buffer}$ = 5 µl min^{-1}), and (*c*) surface treatment with Novec ($\theta > 90^\circ$) results in droplet formation at the T-junction with no aqueous phase adherence to the IP-S surface (Q_{oil} = 6 µl min^{-1}; $Q_{PSI\ buffer}$ = 0.5 µl min^{-1}). For fused silica capillaries: (*d*) Right panel: the aqueous phase co-flows next to the oil (red arrow indicates phase boundary) when flowing both oil and water. The faded line below the red arrow is the same phase boundary from an out-of-focus wall of the capillary (Q_{oil} = 45 µl min^{-1}; $Q_{PSI\ buffer}$ = 5 µl min^{-1}). (*d*) Left panel: an untreated fused silica capillary surface ($\theta < 90^\circ$) with only the aqueous phase which fully wets the walls, provided for comparison. (*e*) After coating a fused silica capillary with Aculon ($\theta < 90^\circ$), aqueous drops adhere to the capillary wall (red arrows indicate adhered drops) (Q_{oil} = 35 µl min^{-1}; $Q_{PSI\ buffer}$ = 5 µl min^{-1}). (*f*) Surface treatment with Novec ($\theta > 90^\circ$) prevents droplets from adhering to the fused silica surface (Q_{oil} = 12 µl min^{-1}; $Q_{mPEG\ buffer}$ = 5 µl min^{-1}). The blue arrow indicates debris on the outside of the capillary. Dashed white lines indicate the cylindrical fused silica capillary walls. The scale bars are 50 µm in all images.

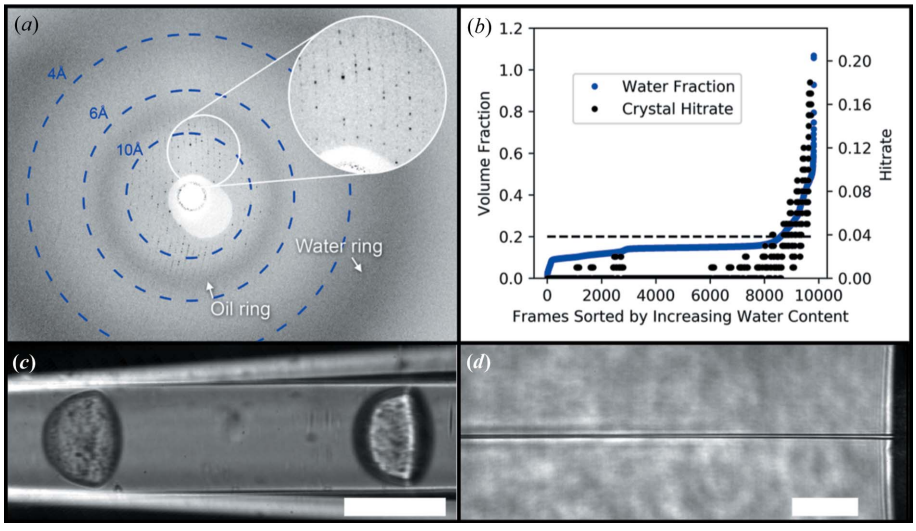

Figure 6
XFEL diffraction from PSI microcrystals injected with a 3D printed microfluidic droplet generation device. (*a*) Single XFEL diffraction pattern showing Bragg diffraction and diffuse scattering from oil (inner ring) and water. Diffraction peaks were observed to ~3.5 Å. (*b*) Volume fraction of water calculated per pattern, sorted by increasing fraction of water (blue). An effective crystal hit rate calculated from binning the sorted patterns into groups of 100 shows a clear correlation between crystal hit rate and water volume fraction. Water fraction values below the dashed line cannot be distinguished from pure oil. (*c*) Droplets containing PSI crystals in an outlet capillary. The capillary was imaged 'free standing' at an angle through the image plane resulting in the right droplet being out of focus. (*d*) Still image of a Novec-coated GDVN jetting oil. Flow rates were 10 µl min^{-1} for PSI buffer solution and 20 µl min^{-1} for oil. Scale bars in (*c*) and (*d*) are 100 µm.

producing droplets that occasionally pinch off approximately at the T-junction and capillary joint, thus preventing control over the droplet generation, as shown in Fig. 5(*b*) for Q_{oil} = 12 µl min^{-1} and $Q_{aqueous}$ = 5 µl min^{-1}. This limitation can be ascribed to the contact angle on the Aculon coating, which does not reach the hydrophobic regime, and to incomplete coverage, low stability of the coating or a combination of these. Lastly, when the surface was treated with Novec, as shown in Fig. 5(*c*) (see video S1 of the supporting information), the aqueous phase did not stream along the wall and instead pinched off into droplets in the device itself (Q_{oil} = 6 µl min^{-1}; $Q_{aqueous}$ = 0.5 µl min^{-1}). This situation was only achieved with a surface treatment capable of rendering the IP-S surface hydrophobic.

Similar effects were observed on fused silica capillary surfaces. When flowing both water and oil phases in untreated surfaces [Fig. 5(*d*), right], the hydrophilic fused silica walls resulted in the aqueous phase flowing as a stream next to the oil phase (Q_{oil} = 45 µl min^{-1}; $Q_{aqueous}$ = 5 µl min^{-1}). When only flowing an aqueous phase, the inner fused silica capillary was fully wetted [Fig. 5(*d*), left]. For cases of contact angles <90° after the surface treatment, or for cases of inhomogeneous surface treatment [Fig. 5(*e*)], a similar situation to that shown in Fig. 5(*b*) is observed in the fused silica capillary (Q_{oil} = 35 µl min^{-1}; $Q_{aqueous}$ = 5 µl min^{-1}). The aqueous phase interacts with the hydrophilic regions and may adhere to the surface. Eventually, a large droplet pinches off from this hydrophilic spot and the droplet progresses until it is captured by the next hydrophilic region. Ultimately, this results in unstable non-uniform droplet generation. Lastly, when the surface is coated with Novec and uniformly hydrophobic [Fig. 5(*f*)], the aqueous droplets do not interact with the walls and maintain their shape, size and spacing (Q_{oil} = 12 µl min^{-1}; $Q_{aqueous}$ = 5 µl min^{-1}). With flow rates in the range

0.5–20 µl min^{-1} for the aqueous phase and 5–40 µl min^{-1} for the oil phase, droplets could be generated for periods of up to 8 h with no observable degradation of the Novec surface coating. Furthermore, droplets containing PSI crystal suspension were generated in a Novec-coated device under similar flow rate conditions [Fig. 6(*c*)]. In this example, <1 nl droplets were generated at a frequency of ∼90 Hz ($Q_{\rm oil}$ = 14 µl min^{-1}; $Q_{\rm aqueous}$ = 3 µl min^{-1}). In addition, the droplets could be transported through capillaries of up to 2 m in length, and the droplet generator was tested at an XFEL as shown in the next section.

3.5. Experimental diffraction from XFELs

To assess the ability to collect XFEL diffraction data using the droplet generator, we performed SFX experiments at the MFX instrument at LCLS (see also Fig. 4 for the entire fluidic setup and the discussion above). The droplet generator was configured for a 120 Hz operation, which is the maximum X-ray pulse repetition rate at LCLS. In these initial tests, droplet synchronization with the XFEL was not realized, although it is the focus of ongoing work. Also, diffraction images were collected at the lower rate of 10 Hz, which is the X-ray detector maximum frequency in 2 × 2 binning mode with an effective pixel size of 89 µm suitable for Bragg peak identification at a detector-to-sample distance of 160 mm.

Microcrystals (0.2–1 µm in size) of the large membrane protein complex PSI were prepared as described previously (Chapman *et al.*, 2011; Hunter & Fromme, 2011) and delivered using the droplet generator as described above. During the run where we observed droplet generation at the beamline with the droplet detector, we were able to collect 10 124 images, of which 94 (1%) were identified as hits by *Cheetah* [see Fig. 6(*a*) for an example diffraction pattern]. Of these 94 images, *CrystFEL* (White *et al.*, 2016) was able to index 46 (50%). The average resolution of these patterns was 6.3 Å, with some patterns showing diffraction peaks to 3.5 Å as estimated by *CrystFEL*. There were not enough higher-resolution images collected to generate a complete data set for structure determination. Initial data analysis showed that the proportion of oil and water in the X-ray-illuminated volume varies from image to image, and correspondingly, the likelihood of hitting a crystal in the water droplet fluctuates as well. This may be attributed to small instabilities in the position of the liquid jet (∼5 µm diameter) when aqueous droplets in oil are injected with reference to the position of the X-ray beam (∼3 µm diameter), resulting in the X-ray beam intersecting the liquid jet in different locations with each XFEL pulse.

In the GDVN, a water droplet carried by the oil stream is focused by a sheath of He gas, leading to droplet stretching. For example, a 0.8 nl droplet could be stretched to a length of 40 mm in a 5 µm diameter jet. This may result in a thin column of water (∼3 µm thick) of finite length enveloped by an oil sheath (∼1 µm thick), additionally contributing to the fluctuation in water content. The likelihood of hitting a crystal in the water droplet also fluctuated, as is commonly observed in SFX experiments with GDVN sample delivery, and as expected for randomly distributed crystals.

In addition, the angle of the liquid jet can flicker between two positions when jetting alternates between only oil or an aqueous droplet, further contributing to varied hit proportions of oil and water. This was observed in laboratory tests and to some extent at the MFX instrument. However, good jet stability when the fluorinated oil was present as shown in Fig. 6(*d*) was observed in the laboratory experiments. Additional detailed characterization of micrometre-scale jets of water in oil suspensions is beyond the scope of this manuscript.

Oil and water scattering patterns are distinguishable by their diffuse rings. As can be seen in Fig. 6(*a*), oil has a relatively narrow diffuse ring with a peak at $q \simeq 8.0$ Å, whereas water has a very broad diffuse ring with a peak at $q \simeq 3.3$ Å. Exposures containing both oil and water may arise when the X-ray pulse hits the spheroidal end of a droplet. Furthermore, as described above, a thin layer of oil around the droplets prevents wetting of the capillary walls (hence the hydrophobic surface treatment) which may extend into the liquid jet and interaction region causing simultaneous exposure of oil and water. Several example images of diffraction patterns in varying fractions of oil/water are shown in Fig. S2 of the supporting information. A correlation between the diffraction resolution limit and volume fraction of water was not observed. To assess the correlation between the likelihood of hitting a crystal and the volume fraction of water illuminated by the X-ray beam (and thus successful droplet generation), we analyzed the one-dimensional radial scattering profiles calculated for each image. Using oil-only and water-only scattering profiles, the volume fractions of oil and water in each image were estimated using a simple linear combination fitting procedure [Fig. 6(*b*)]. Owing to the diffuse nature of the oil and water rings, low volume fractions of water below ∼20% [dashed line in Fig. 6(*b*)] cannot be distinguished from pure oil. This probably refers to the regime where synchronization between the droplet generator and the XFEL pulse sequence is not achieved. After sorting the images by increasing the volume fraction of water, crystal hit rates were calculated by binning the images into groups of 100 and calculating the average hit rate within each group. The results show a clear correlation between the effective crystal hit rate and the increasing volume fraction of water [Fig. 6(*b*)], and correspondingly successful droplet generation. This demonstrates that, despite the lack of synchronization of droplets with the X-ray pulses in this prototype, the 3D printed droplet generation device successfully injected crystal-containing aqueous droplets into the oil stream, and delivered the resulting liquid jet into the X-ray beam path for serial microcrystallography data collection.

4. Conclusions

Current liquid injection methods for SFX typically waste the majority of injected crystals as a result of the mismatch between XFEL pulse repetition rate and jet speed. Because of

this mismatch, most of the sample flows into waste without interacting with the X-ray beam. We address this problem with a microfluidic droplet generator that effectively stops the flow of sample between X-ray pulses by interleaving crystal-laden aqueous droplets within an oil jet. Our device consists of a 3D printed T-junction droplet generator coupled to fused silica capillaries interfacing with liquid handling periphery and sample injectors. The wetting properties of bare 3D printed devices did not allow reproducible droplet generation. We therefore investigated the effect of the two commercially available coatings Novec and Aculon as well as gas phase silanization with TDTS in the performance of the droplet in oil generation. While the two commercially available coatings can be applied by simple filling methods, the gas phase silanization method was impractical for this application because of the intricate geometry and small dimensions of the surfaces that need to be coated. Of the three surface treatments investigated under conditions mimicking the flow in an XFEL experiment, Novec provided the most hydrophobic surface and most stable coating on both photoresist films and glass. Importantly, we demonstrated that Novec-treated droplet generation devices produce stable droplets of aqueous buffers employed in an SFX experiment over several hours, suitable for use in an entire shift at an XFEL facility. In contrast, coatings rendering lower hydrophobicity resulted in flow conditions unsuitable for robust droplet generation such as co-flowing of the oil and aqueous phases, intermittent surface attachment of the aqueous phase or random droplet generation. We also demonstrated the successful application of the novel droplet generator at an SFX experiment at LCLS and showed a correlation between crystal hit rate and volume fraction of water during droplet generation. Robust droplet generation with a 3D printed device and Novec surface coatings will be utilized for the synchronization of crystal suspension droplets with the frequency and phase of XFELs in the future.

Acknowledgements

We thank Stella Lisova in the Physics Department of Arizona State University for fruitful discussions and technical assistance, and Chufeng Li for help with data collection and monitoring.

Funding information

This work was supported by the STC Program of the National Science Foundation (NSF) through BioXFEL (agreement No. 1231306), NSF DBI (award No. 1565180) and the National Institutes of Health (award No. R01GM095583). We further thank 3M for the kind donation of Novec 1720. Use of the Linac Coherent Light Source (LCLS), SLAC National Accelerator Laboratory, is supported by the US Department of Energy, Office of Science, Office of Basic Energy Sciences (contract No. DE-AC02-76SF00515). The HERA system for in-helium experiments at MFX was developed by Dr Bruce Doak and funded by the Max-Planck Institute for Medical Research in Heidelberg, Germany. JCV gratefully acknowledges financial support through a CONACYT fellowship.

References

Abdallah, B. G., Chao, T. C., Kupitz, C., Fromme, P. & Ros, A. (2013). *ACS Nano*, **7**, 9129–9137.

Abdallah, B. G., Zatsepin, N. A., Roy-Chowdhury, S., Coe, J., Conrad, C. E., Dörner, K., Sierra, R. G., Stevenson, H. P., Camacho-Alanis, F., Grant, T. D., Nelson, G., James, D., Calero, G., Wachter, R. M., Spence, J. C., Weierstall, U., Fromme, P. & Ros, A. (2015). *Struct. Dyn.* **2**, 041719.

Aghvami, S. A., Opathalage, A., Zhang, Z. K., Ludwig, M., Heymann, M., Norton, M., Wilkins, N. & Fraden, S. (2017). *Sens. Actuators B Chem.* **247**, 940–949.

Barty, A., Kirian, R. A., Maia, F. R. N. C., Hantke, M., Yoon, C. H., White, T. A. & Chapman, H. (2014). *J. Appl. Cryst.* **47**, 1118–1131.

Beyerlein, K. R., Adriano, L., Heymann, M., Kirian, R., Knoška, J., Wilde, F., Chapman, H. N. & Bajt, S. (2015). *Rev. Sci. Instrum.* **86**, 125104.

Bohne, S., Heymann, M., Chapman, H. N., Trieu, H. K. & Bajt, S. (2019). *Rev. Sci. Instrum.* **90**, 035108.

Boutet, S., Cohen, A. E. & Wakatsuki, S. (2016). *Synchrotron Radiat. News*, **29**, 23–28.

Calvey, G. D., Katz, A. M., Schaffer, C. B. & Pollack, L. (2016). *Struct. Dyn.* **3**, 054301.

Campo, A. del & Greiner, C. (2007). *J. Micromech. Microeng.* **17**, R81-R95.

Chae, S. K., Lee, C. H., Lee, S. H., Kim, T. S. & Kang, J. Y. (2009). *Lab Chip*, **9**, 1957–1961.

Chapman, H. N., Fromme, P., Barty, A., White, T. A., Kirian, R. A., Aquila, A., Hunter, M. S., Schulz, J., DePonte, D. P., Weierstall, U., Doak, R. B., Maia, F. R., Martin, A. V., Schlichting, I., Lomb, L., Coppola, N., Shoeman, R. L., Epp, S. W., Hartmann, R., Rolles, D., Rudenko, A., Foucar, L., Kimmel, N., Weidenspointner, G., Holl, P., Liang, M., Barthelmess, M., Caleman, C., Boutet, S., Bogan, M. J., Krzywinski, J., Bostedt, C., Bajt, S., Gumprecht, L., Rudek, B., Erk, B., Schmidt, C., Hömke, A., Reich, C., Pietschner, D., Strüder, L., Hauser, G., Gorke, H., Ullrich, J., Herrmann, S., Schaller, G., Schopper, F., Soltau, H., Kühnel, K. U., Messerschmidt, M., Bozek, J. D., Hau-Riege, S. P., Frank, M., Hampton, C. Y., Sierra, R. G., Starodub, D., Williams, G. J., Hajdu, J., Timneanu, N., Seibert, M. M., Andreasson, J., Rocker, A., Jönsson, O., Svenda, M., Stern, S., Nass, K., Andritschke, R., Schröter, C. D., Krasniqi, F., Bott, M., Schmidt, K. E., Wang, X., Grotjohann, I., Holton, J. M., Barends, T. R., Neutze, R., Marchesini, S., Fromme, R., Schorb, S., Rupp, D., Adolph, M., Gorkhover, T., Andersson, I., Hirsemann, H., Potdevin, G., Graafsma, H., Nilsson, B. & Spence, J. C. (2011). *Nature*, **470**, 73–77.

Chavas, L. M., Gumprecht, L. & Chapman, H. N. (2015). *Struct. Dyn.* **2**, 041709.

Conrad, C. E., Basu, S., James, D., Wang, D., Schaffer, A., Roy-Chowdhury, S., Zatsepin, N. A., Aquila, A., Coe, J., Gati, C., Hunter, M. S., Koglin, J. E., Kupitz, C., Nelson, G., Subramanian, G., White, T. A., Zhao, Y., Zook, J., Boutet, S., Cherezov, V., Spence, J. C. H., Fromme, R., Weierstall, U. & Fromme, P. (2015). *IUCrJ*, **2**, 421–430.

Doak, R., DePonte, D., Nelson, G., Camacho-Alanis, F., Ros, A., Spence, J. & Weierstall, U. (2012). *AIP Conf. Proc.* **1501**, 1314–1323.

Duong, T. T., Kim, G., Ros, R., Streek, M., Schmid, F., Brugger, J., Anselmetti, D. & Ros, A. (2003). *Microelectron. Eng.* **67–68**, 905–912.

Echelmeier, A., Nelson, G., Abdallah, B. G., James, D., Roy-Chowdhury, S., Tolstikova, A., Mariani, V., Kirian, R. A., Oberthüer, D., Dörner, K., Fromme, P., Chapman, H. N., Weierstall, U., Spence, J. C. H. & Ros, A. (2015). *Proceedings of the 19th International Conference on Miniaturized Systems for Chemistry*

and Life Sciences (MicroTAS2015), pp. 1374–1376. Red Hook: Curran Associates/Chemical and Biological Microsystems Society.
Fadeev, A. Y. & Kazakevich, Y. V. (2002). *Langmuir*, **18**, 2665–2672.
Ferreira, J., Castro, F., Rocha, F. & Kuhn, S. (2018). *Chem. Eng. Sci.* **191**, 232–244.
Fuller, F. D., Gul, S., Chatterjee, R., Burgie, E. S., Young, I. D., Lebrette, H., Srinivas, V., Brewster, A. S., Michels-Clark, T., Clinger, J. A., Andi, B., Ibrahim, M., Pastor, E., de Lichtenberg, C., Hussein, R., Pollock, C. J., Zhang, M., Stan, C. A., Kroll, T., Fransson, T., Weninger, C., Kubin, M., Aller, P., Lassalle, L., Bräuer, P., Miller, M. D., Amin, M., Koroidov, S., Roessler, C. G., Allaire, M., Sierra, R. G., Docker, P. T., Glownia, J. M., Nelson, S., Koglin, J. E., Zhu, D., Chollet, M., Song, S., Lemke, H., Liang, M., Sokaras, D., Alonso-Mori, R., Zouni, A., Messinger, J., Bergmann, U., Boal, A. K., Bollinger, J. M. Jr, Krebs, C., Högbom, M., Phillips, G. N. Jr, Vierstra, R. D., Sauter, N. K., Orville, A. M., Kern, J., Yachandra, V. K. & Yano, J. (2017). *Nat. Methods*, **14**, 443–449.
Garstecki, P., Fuerstman, M. J., Stone, H. A. & Whitesides, G. M. (2006). *Lab Chip*, **6**, 437–446.
Ghazal, A., Lafleur, J. P., Mortensen, K., Kutter, J. P., Arleth, L. & Jensen, G. V. (2016). *Lab Chip*, **16**, 4263–4295.
Guzowski, J., Gizynski, K., Gorecki, J. & Garstecki, P. (2016). *Lab Chip*, **16**, 764–772.
Heymann, M., Opthalage, A., Wierman, J. L., Akella, S., Szebenyi, D. M. E., Gruner, S. M. & Fraden, S. (2014). *IUCrJ*, **1**, 349–360.
Ho, C. M., Ng, S. H., Li, K. H. & Yoon, Y. J. (2015). *Lab Chip*, **15**, 3627–3637.
Huang, T. Y., Sakar, M. S., Mao, A., Petruska, A. J., Qiu, F., Chen, X. B., Kennedy, S., Mooney, D. & Nelson, B. J. (2015). *Adv. Mater.* **27**, 6644–6650.
Hunter, M. S. & Fromme, P. (2011). *Methods*, **55**, 387–404.
Hunter, M. S., Segelke, B., Messerschmidt, M., Williams, G. J., Zatsepin, N. A., Barty, A., Benner, W. H., Carlson, D. B., Coleman, M., Graf, A., Hau-Riege, S. P., Pardini, T., Seibert, M. M., Evans, J., Boutet, S. & Frank, M. (2014). *Sci. Rep.* **4**, 6026.
Hunter, M. S. & Sublett, B. (2019). *Sample Delivery Methods*, https://lcls.slac.stanford.edu/sed/methods.
Husny, J. & Cooper-White, J. J. (2006). *J. Non-Newt. Fluid Mech.* **137**, 121–136.
Kirchner, R., Chidambaram, N., Altana, M. & Schift, H. (2017). *Proc. SPIE*, **10095**, 1009507.
Kuhn, S., Hartman, R. L., Sultana, M., Nagy, K. D., Marre, S. & Jensen, K. F. (2011). *Langmuir*, **27**, 6519–6527.
Lee, K. S., Kim, R. H., Yang, D. Y. & Park, S. H. (2008). *Prog. Polym. Sci.* **33**, 631–681.
Li, L. & Ismagilov, R. F. (2010). *Annu. Rev. Biophys.* **39**, 139–158.
Ligon, S. C., Liska, R., Stampfl, J., Gurr, M. & Mülhaupt, R. (2017). *Chem. Rev.* **117**, 10212–10290.
Lomb, L., Steinbrener, J., Bari, S., Beisel, D., Berndt, D., Kieser, C., Lukat, M., Neef, N. & Shoeman, R. L. (2012). *J. Appl. Cryst.* **45**, 674–678.
Lyubimov, A. Y., Murray, T. D., Koehl, A., Araci, I. E., Uervirojnangkoorn, M., Zeldin, O. B., Cohen, A. E., Soltis, S. M., Baxter, E. L., Brewster, A. S., Sauter, N. K., Brunger, A. T. & Berger, J. M. (2015). *Acta Cryst.* D**71**, 928–940.
Maeki, M., Yamaguchi, H., Tokeshi, M. & Miyazaki, M. (2016). *Anal. Sci.* **32**, 3–9.
Mafuné, F., Miyajima, K., Tono, K., Takeda, Y., Kohno, J., Miyauchi, N., Kobayashi, J., Joti, Y., Nango, E., Iwata, S. & Yabashi, M. (2016). *Acta Cryst.* D**72**, 520–523.
Mariani, V., Morgan, A., Yoon, C. H., Lane, T. J., White, T. A., O'Grady, C., Kuhn, M., Aplin, S., Koglin, J., Barty, A. & Chapman, H. N. (2016). *J. Appl. Cryst.* **49**, 1073–1080.
Martiel, I., Müller-Werkmeister, H. M. & Cohen, A. E. (2019). *Acta Cryst.* D**75**, 160–177.
Martinelli, E., Agostini, S., Galli, G., Chiellini, E., Glisenti, A., Pettitt, M. E., Callow, M. E., Callow, J. A., Graf, K. & Bartels, F. W. (2008). *Langmuir*, **24**, 13138–13147.
Martin-Garcia, J. M., Conrad, C. E., Coe, J., Roy-Chowdhury, S. & Fromme, P. (2016). *Arch. Biochem. Biophys.* **602**, 32–47.
Mathews, I. I., Allison, K., Robbins, T., Lyubimov, A. Y., Uervirojnangkoorn, M., Brunger, A. T., Khosla, C., DeMirci, H., McPhillips, S. E., Hollenbeck, M., Soltis, M. & Cohen, A. E. (2017). *Biochemistry*, **56**, 4751–4756.
Mueller, C., Marx, A., Epp, S. W., Zhong, Y., Kuo, A., Balo, A. R., Soman, J., Schotte, F., Lemke, H. T., Owen, R. L., Pai, E. F., Pearson, A. R., Olson, J. S., Anfinrud, P. A., Ernst, O. P. & Dwayne Miller, R. J. (2015). *Struct. Dyn.* **2**, 054302.
Murray, T. D., Lyubimov, A. Y., Ogata, C. M., Vo, H., Uervirojnangkoorn, M., Brunger, A. T. & Berger, J. M. (2015). *Acta Cryst.* D**71**, 1987–1997.
Nelson, G., Kirian, R. A., Weierstall, U., Zatsepin, N. A., Faragó, T., Baumbach, T., Wilde, F., Niesler, F. B., Zimmer, B., Ishigami, I., Hikita, M., Bajt, S., Yeh, S. R., Rousseau, D. L., Chapman, H. N., Spence, J. C. & Heymann, M. (2016). *Opt. Express*, **24**, 11515–11530.
Nge, P. N., Rogers, C. I. & Woolley, A. T. (2013). *Chem. Rev.* **113**, 2550–2583.
Nisisako, T., Torii, T. & Higuchi, T. (2002). *Lab Chip*, **2**, 24–26.
Oberthuer, D., Knoška, J., Wiedorn, M. O., Beyerlein, K. R., Bushnell, D. A., Kovaleva, E. G., Heymann, M., Gumprecht, L., Kirian, R. A., Barty, A., Mariani, V., Tolstikova, A., Adriano, L., Awel, S., Barthelmess, M., Dörner, K., Xavier, P. L., Yefanov, O., James, D. R., Nelson, G., Wang, D., Calvey, G., Chen, Y., Schmidt, A., Szczepek, M., Frielingsdorf, S., Lenz, O., Snell, E., Robinson, P. J., Šarler, B., Belšak, G., Maček, M., Wilde, F., Aquila, A., Boutet, S., Liang, M., Hunter, M. S., Scheerer, P., Lipscomb, J. D., Weierstall, U., Kornberg, R. D., Spence, J. C. H., Pollack, L., Chapman, H. N. & Bajt, S. (2017). *Sci. Rep.* **7**, 44628.
Quéré, D. (2008). *Annu. Rev. Mater. Res.* **38**, 71–99.
Riche, C. T., Zhang, C., Gupta, M. & Malmstadt, N. (2014). *Lab Chip*, **14**, 1834–1841.
Roedig, P., Ginn, H. M., Pakendorf, T., Sutton, G., Harlos, K., Walter, T. S., Meyer, J., Fischer, P., Duman, R., Vartiainen, I., Reime, B., Warmer, M., Brewster, A. S., Young, I. D., Michels-Clark, T., Sauter, N. K., Kotecha, A., Kelly, J., Rowlands, D. J., Sikorsky, M., Nelson, S., Damiani, D. S., Alonso-Mori, R., Ren, J., Fry, E. E., David, C., Stuart, D. I., Wagner, A. & Meents, A. (2017). *Nat. Methods*, **14**, 805–810.
Roessler, C. G., Agarwal, R., Allaire, M., Alonso-Mori, R., Andi, B., Bachega, J. F. R., Bommer, M., Brewster, A. S., Browne, M. C., Chatterjee, R., Cho, E., Cohen, A. E., Cowan, M., Datwani, S., Davidson, V. L., Defever, J., Eaton, B., Ellson, R., Feng, Y., Ghislain, L. P., Glownia, J. M., Han, G., Hattne, J., Hellmich, J., Héroux, A., Ibrahim, M., Kern, J., Kuczewski, A., Lemke, H. T., Liu, P., Majlof, L., McClintock, W. M., Myers, S., Nelsen, S., Olechno, J., Orville, A. M., Sauter, N. K., Soares, A. S., Soltis, S. M., Song, H., Stearns, R. G., Tran, R., Tsai, Y., Uervirojnangkoorn, M., Wilmot, C. M., Yachandra, V., Yano, J., Yukl, E. T., Zhu, D. & Zouni, A. (2016). *Structure*, **24**, 631–640.
Saini, G., Sautter, K., Hild, F. E., Pauley, J. & Linford, M. R. (2008). *J. Vac. Sci. Technol. A*, **26**, 1224–1234.
Sarvothaman, M. K., Kim, K. S., Seale, B., Brodersen, P. M., Walker, G. C. & Wheeler, A. R. (2015). *Adv. Funct. Mater.* **25**, 506–515.
Scheler, O., Kaminski, T. S., Ruszczak, A. & Garstecki, P. (2016). *Appl. Mater. Interfaces*, **8**, 11318–11325.
Seddon, E. A., Clarke, J. A., Dunning, D. J., Masciovecchio, C., Milne, C. J., Parmigiani, F., Rugg, D., Spence, J. C. H., Thompson, N. R., Ueda, K., Vinko, S. M., Wark, J. S. & Wurth, W. (2017). *Rep. Prog. Phys.* **80**, 115901.
Seemann, R., Brinkmann, M., Pfohl, T. & Stephan, H. (2012). *Rep. Prog. Phys.* **75**, 016601.
Sierra, R. G., Batyuk, A., Sun, Z., Aquila, A., Hunter, M. S., Lane, T. J., Liang, M., Yoon, C. H., Alonso-Mori, R., Armenta, R., Castagna, J.-C., Hollenbeck, M., Osier, T. O., Hayes, M., Aldrich, J., Curtis, R., Koglin, J. E., Rendahl, T., Rodriguez, E., Carbajo, S., Guillet, S.,

Paul, R., Hart, P., Nakahara, K., Carini, G., DeMirci, H., Dao, E. H., Hayes, B. M., Rao, Y. P., Chollet, M., Feng, Y., Fuller, F. D., Kupitz, C., Sato, T., Seaberg, M. H., Song, S., van Driel, T. B., Yavas, H., Zhu, D., Cohen, A. E., Wakatsuki, S. & Boutet, S. (2019). *J. Synchrotron Rad.* **26**, 346–357.

Sierra, R. G., Gati, C., Laksmono, H., Dao, E. H., Gul, S., Fuller, F., Kern, J., Chatterjee, R., Ibrahim, M., Brewster, A. S., Young, I. D., Michels-Clark, T., Aquila, A., Liang, M., Hunter, M. S., Koglin, J. E., Boutet, S., Junco, E. A., Hayes, B., Bogan, M. J., Hampton, C. Y., Puglisi, E. V., Sauter, N. K., Stan, C. A., Zouni, A., Yano, J., Yachandra, V. K., Soltis, S. M., Puglisi, J. D. & DeMirci, H. (2016). *Nat. Methods*, **13**, 59–62.

Song, H. & Ismagilov, R. F. (2003). *J. Am. Chem. Soc.* **125**, 14613–14619.

Song, H., Tice, J. D. & Ismagilov, R. F. (2003). *Angew. Chem. Int. Ed.* **42**, 768–772.

Sugahara, M., Mizohata, E., Nango, E., Suzuki, M., Tanaka, T., Masuda, T., Tanaka, R., Shimamura, T., Tanaka, Y., Suno, C., Ihara, K., Pan, D., Kakinouchi, K., Sugiyama, S., Murata, M., Inoue, T., Tono, K., Song, C., Park, J., Kameshima, T., Hatsui, T., Joti, Y., Yabashi, M. & Iwata, S. (2015). *Nat. Methods*, **12**, 61–63.

Sugahara, M., Song, C., Suzuki, M., Masuda, T., Inoue, S., Nakane, T., Yumoto, F., Nango, E., Tanaka, R., Tono, K., Joti, Y., Kameshima, T., Hatsui, T., Yabashi, M., Nureki, O., Numata, K. & Iwata, S. (2016). *Sci. Rep.* **6**, 24484.

Teh, S. Y., Lin, R., Hung, L. H. & Lee, A. P. (2008). *Lab Chip*, **8**, 198–220.

Thorsen, T., Roberts, R. W., Arnold, F. H. & Quake, S. R. (2001). *Phys. Rev. Lett.* **86**, 4163–4166.

Tono, K. (2017). *High Power Laser Sci. Eng.* **5**, e7.

Tono, K., Nango, E., Sugahara, M., Song, C., Park, J., Tanaka, T., Tanaka, R., Joti, Y., Kameshima, T., Ono, S., Hatsui, T., Mizohata, E., Suzuki, M., Shimamura, T., Tanaka, Y., Iwata, S. & Yabashi, M. (2015). *J. Synchrotron Rad.* **22**, 532–537.

Trebbin, M., Krüger, K., DePonte, D., Roth, S. V., Chapman, H. N. & Förster, S. (2014). *Lab Chip*, **14**, 1733–1745.

Tullis, J., Park, C. L. & Abbyad, P. (2014). *Lab Chip*, **14**, 3285–3289.

Waheed, S., Cabot, J. M., Macdonald, N. P., Lewis, T., Guijt, R. M., Paull, B. & Breadmore, M. C. (2016). *Lab Chip*, **16**, 1993–2013.

Wang, D. (2014). PhD thesis, Arizona State University, USA.

Weierstall, U. (2014). *Philos. Trans. R. Soc. London B Biol. Sci.* **369**, 20130337.

White, T. A., Mariani, V., Brehm, W., Yefanov, O., Barty, A., Beyerlein, K. R., Chervinskii, F., Galli, L., Gati, C., Nakane, T., Tolstikova, A., Yamashita, K., Yoon, C. H., Diederichs, K. & Chapman, H. N. (2016). *J. Appl. Cryst.* **49**, 680–689.

Wiedorn, M. O., Oberthür, D., Bean, R., Schubert, R., Werner, N., Abbey, B., Aepfelbacher, M., Adriano, L., Allahgholi, A., Al-Qudami, N., Andreasson, J., Aplin, S., Awel, S., Ayyer, K., Bajt, S., Barák, I., Bari, S., Bielecki, J., Botha, S., Boukhelef, D., Brehm, W., Brockhauser, S., Cheviakov, I., Coleman, M. A., Cruz-Mazo, F., Danilevski, C., Darmanin, C., Doak, R. B., Domaracky, M., Dörner, K., Du, Y., Fangohr, H., Fleckenstein, H., Frank, M., Fromme, P., Gañán-Calvo, A. M., Gevorkov, Y., Giewekemeyer, K., Ginn, H. M., Graafsma, H., Graceffa, R., Greiffenberg, D., Gumprecht, L., Göttlicher, P., Hajdu, J., Hauf, S., Heymann, M., Holmes, S., Horke, D. A., Hunter, M. S., Imlau, S., Kaukher, A., Kim, Y., Klyuev, A., Knoška, J., Kobe, B., Kuhn, M., Kupitz, C., Küpper, J., Lahey-Rudolph, J. M., Laurus, T., Le Cong, K., Letrun, R., Xavier, P. L., Maia, L., Maia, F., Mariani, V., Messerschmidt, M., Metz, M., Mezza, D., Michelat, T., Mills, G., Monteiro, D. C. F., Morgan, A., Mühlig, K., Munke, A., Münnich, A., Nette, J., Nugent, K. A., Nuguid, T., Orville, A. M., Pandey, S., Pena, G., Villanueva-Perez, P., Poehlsen, J., Previtali, G., Redecke, L., Riekehr, W. M., Rohde, H., Round, A., Safenreiter, T., Sarrou, I., Sato, T., Schmidt, M., Schmitt, B., Schönherr, R., Schulz, J., Sellberg, J. A., Seibert, M. M., Seuring, C., Shelby, M. L., Shoeman, R. L., Sikorski, M., Silenzi, A., Stan, C. A., Shi, X., Stern, S., Sztuk-Dambietz, J., Szuba, J., Tolstikova, A., Trebbin, M., Trunk, U., Vagovic, P., Ve, T., Weinhausen, B., White, T. A., Wrona, K., Xu, C., Yefanov, O., Zatsepin, N., Zhang, J., Perbandt, M., Mancuso, A. P., Betzel, C., Chapman, H. & Barty, A. (2018). *Nat. Commun.* **9**, 4025.

Wong, I. & Ho, C. M. (2009). *Microfluid Nanofluidics*, **7**, 291–306.

Yang, C., Tartaglino, U. & Persson, B. N. (2008). *Eur. Phys. J. E Soft Matter*, **25**, 139–152.

Yang, F. C., Chen, X. P. & Yue, P. T. (2018). *Phys. Fluids*, **30**, 012106.

Zhang, S. H., Guivier-Curien, C., Veesler, S. & Candoni, N. (2015). *Chem. Eng. Sci.* **138**, 128–139.

Zheng, B., Roach, L. S. & Ismagilov, R. F. (2003). *J. Am. Chem. Soc.* **125**, 11170–11171.

Zheng, B., Tice, J. D., Roach, L. S. & Ismagilov, R. F. (2004). *Angew. Chem. Int. Ed.* **43**, 2508–2511.

Zhu, P. & Wang, L. (2016). *Lab Chip*, **17**, 34–75.